



This is a repository copy of *Time-resolved x-ray absorption spectroscopy with a water window high-harmonic source*.

White Rose Research Online URL for this paper:

<https://eprints.whiterose.ac.uk/110214/>

Version: Accepted Version

Article:

Pertot, Y., Schmidt, C., Matthews, M. et al. (8 more authors) (2017) Time-resolved x-ray absorption spectroscopy with a water window high-harmonic source. *Science*, 355 (6322). pp. 264-267. ISSN 0036-8075

<https://doi.org/10.1126/science.aah6114>

Reuse

Items deposited in White Rose Research Online are protected by copyright, with all rights reserved unless indicated otherwise. They may be downloaded and/or printed for private study, or other acts as permitted by national copyright laws. The publisher or other rights holders may allow further reproduction and re-use of the full text version. This is indicated by the licence information on the White Rose Research Online record for the item.

Takedown

If you consider content in White Rose Research Online to be in breach of UK law, please notify us by emailing eprints@whiterose.ac.uk including the URL of the record and the reason for the withdrawal request.



eprints@whiterose.ac.uk
<https://eprints.whiterose.ac.uk/>

Time-resolved X-ray absorption spectroscopy with a water-window high-harmonic source

Yoann Pertot¹, Cédric Schmidt², Mary Matthews^{1,2}, Adrien Chauvet², Martin Huppert¹, Vit Svoboda¹, Aaron von Conta¹, Andres Tehlar¹, Denitsa Baykusheva¹, Jean-Pierre Wolf² and Hans Jakob Wörner^{1*}

¹Laboratorium für Physikalische Chemie, ETH Zürich, Zurich, Switzerland

²GAP-Biophotonics, Université de Genève, Geneva, Switzerland

*Corresponding author: hwoerner@ethz.ch; www.atto.ethz.ch.

Time-resolved X-ray absorption spectroscopy (TR-XAS) has so far practically been limited to large-scale facilities, to sub-picosecond temporal resolution and to the condensed phase. Here, we report the realization of TR-XAS with a temporal resolution in the low femtosecond range by developing a table-top high-harmonic source reaching up to 350 eV, thus partially covering the spectral region of 280 to 530 eV, where water is transmissive. We use this source to follow previously unexamined light-induced chemical reactions in the lowest electronic states of isolated CF_4^+ and SF_6^+ molecules in the gas phase. By probing element-specific core-to-valence transitions at the carbon K-edge or the sulfur L-edges, we characterize their reaction paths and observe the effect of symmetry breaking through the splitting of absorption bands and Rydberg-valence mixing induced by the geometry changes.

The application of X-ray sources to the study of the structure of matter has led to some of the most prominent advances in science in the 20th century, be it by diffraction (1) or spectroscopy (2). In the 21st century, the temporal dimension has been added to X-ray measurements, both at synchrotrons (3) and through the recent development of free-electron lasers (4–7). In parallel to these efforts, incoherent table-top hard X-ray sources have been applied to picosecond time-resolved studies (8,9). An alternative approach to generating soft X-rays with the advantages of full temporal and spatial coherence, as well as perfect temporal synchronization, is provided by high-harmonic generation. Very early efforts were successful at generating a modest soft-X-ray flux from titanium:sapphire drivers (10–12). Considerable progress came through the extension to longer-wavelength drivers (13–18). However, time-resolved measurements with such sources have so far remained out of reach.

Here, we describe a femtosecond time-resolved experiment using soft-X-ray supercontinua reaching into the water window. Using a long-wavelength driver (1.8 μm) with exceptional average power (2.5 W, i.e. 2.5 mJ at 1 kHz), we generate soft-X-ray supercontinua ranging from 100 to 350 eV, thus covering the chemically and biologically important K-edge of carbon. We use this source to study dissociation reactions of molecular cations, that have previously not been resolved in time, by transient absorption at the K-edge of carbon and all L-edges of sulfur simultaneously. This development considerably extends pioneering work on transient absorption in the extreme ultraviolet (19–22). These studies were limited to photon energies below ~ 100 eV, and therefore to the L-edge of silicon and the M- and N-edges of heavier elements.

Our measurements probe the spatial structure of unoccupied orbitals and associated changes along the photochemical reaction pathways. Exploiting the sensitivity of X-ray absorption near-edge structure (XANES) spectroscopy to chemical shifts, we follow the evolution of the unoccupied valence orbitals of molecules from the neutral to the cation and along the reaction path to the final products. Using the sensitivity of dipole selection rules to molecular symmetry, we observe a splitting of some of the initially triply-degenerate orbitals of CF_4 and SF_6 to doubly- or non-degenerate orbitals as a consequence of the symmetry lowering induced by photodissociation.

In the experiment we focus a mid-infrared (MIR) femtosecond pulse centered at 1.8 μm into

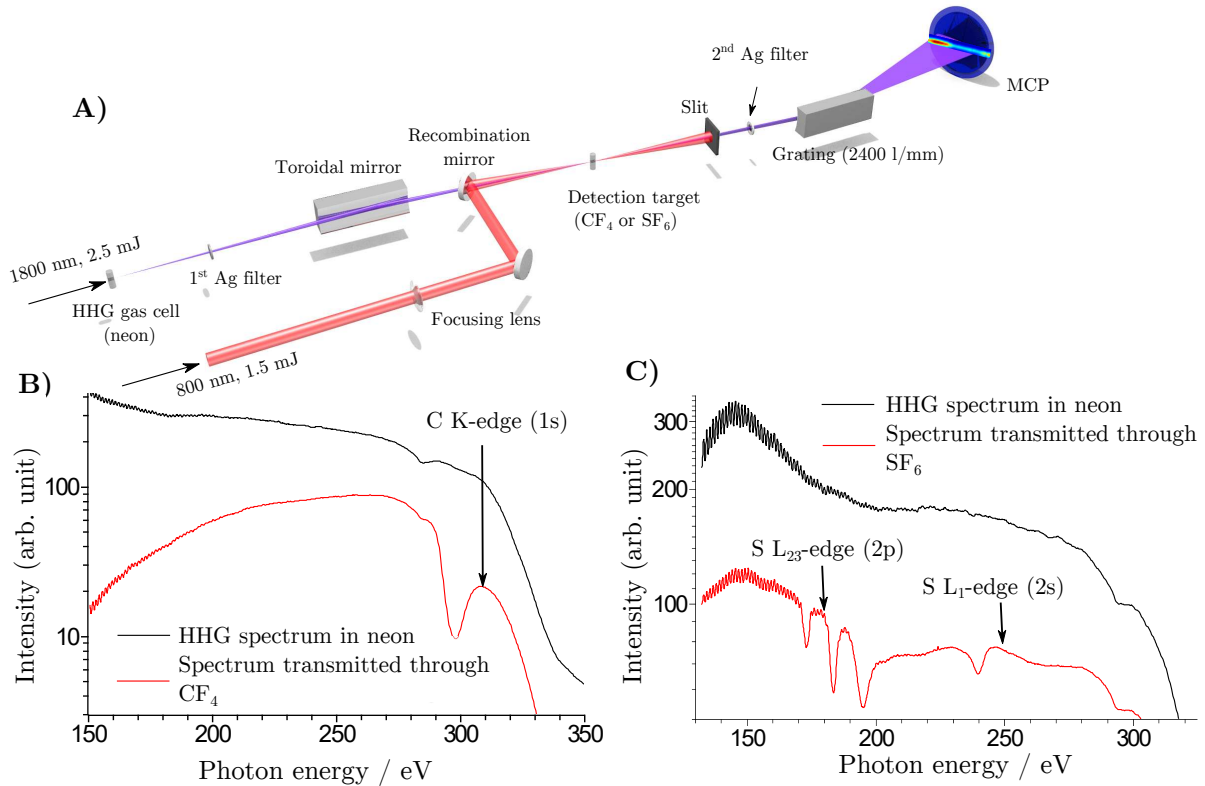


Figure 1: **Soft-X-ray transient-absorption spectroscopy with a high-harmonic source** A) Experimental setup, B) High-harmonic spectrum at the carbon K-edge and transmitted spectrum through CF_4 gas, C) High-harmonic spectrum at the sulfur L-edges and transmitted spectrum through SF_6 gas.

a differentially-pumped high-pressure neon gas cell (Fig. 1A). A toroidal mirror images the soft X-ray (SXR) generation region into a target-gas cell where it is superimposed with a near-infrared (NIR) pulse centered at 800 nm. The SXR absorption of CF_4 (Fig. 1B) is dominated by overlapping transitions from the carbon 1s shell to the $5t_2$ and $6t_2$ unoccupied orbitals of dominant σ^* character that peak at 298 eV. These assignments are based on our time-dependent density-functional theory (TDDFT) calculations of core-shell absorption spectra that use the LB94 functional and the QZ4P basis set (valence quadruple zeta + 4 polarization functions, relativistically optimized) and are consistent with high-resolution spectra recorded at synchrotron facilities (23). The SXR absorption spectrum of SF_6 (Fig. 1C) is dominated by transitions from the sulfur $2p_{1/2}$ and $2p_{3/2}$ shells to the a_{1g} unoccupied orbital and to the shape resonances of t_{2g} and e_g symmetry lying above the $L_{2,3}$ -edge. A weaker absorption feature at ~ 240 eV is as-

signed to the transition from the sulfur 2s shell to the anti-bonding orbital of t_{1u} symmetry, lying just below the L_1 edge, which is also consistent with the synchrotron literature (24). The weak modulation observed in both spectra up to energies of ~ 180 eV corresponds to harmonic structure. The experimentally determined resolution of $E/\Delta E = 308$ suggests that the appearance of these spectra is not spectrometer limited.

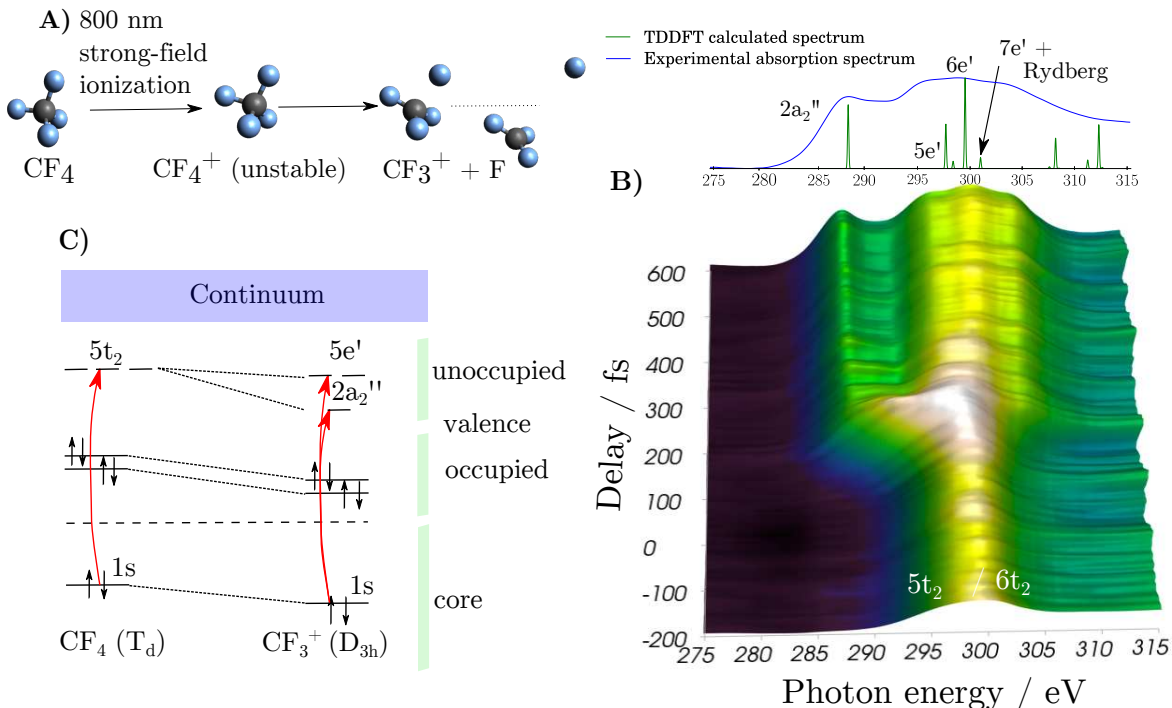


Figure 2: **Transient-absorption spectroscopy at the carbon K-edge** A) An intense near-infrared pulse induces single ionization of CF_4 to CF_4^+ which is unstable in its electronic ground state and dissociates into $\text{CF}_3^+ + \text{F}$. The sequence of geometries is taken from a calculated minimum-energy reaction path (see text for details). B) Absorbance ($A(t) = \ln(I_0/I(t))$) as a function of the SXR-NIR time delay. Negative time delays correspond to the SXR pulse preceding the NIR pulse. The intensity axis, as well as the color scale, are linear. The standard deviation of this data set amounts to 4%. The calculated stick spectrum in the inset has been shifted by -2.5 eV. C) Orbital diagram illustrating selected transitions, as obtained from TDDFT/LB94 calculations.

Strong-field ionization of neutral CF_4 in the gas phase is induced by an ultrashort NIR pulse centered at 800 nm, focused to a peak intensity of $(4 - 5) \times 10^{14}$ W/cm². Ionization of CF_4 to each of the three lowest-lying electronic states of CF_4^+ , of respective vertical ionization energies 16.29, 17.51 and 18.54 eV (measured from the neutral ground state) (25), results in spontaneous

dissociation into CF_3^+ and F (26). At positive delays, an increase of the absorbance and a red shift of its maximum are observed in the TR-XAS spectra (Fig. 2B). After reaching a maximal absorbance, the absorption spectrum progressively splits into multiple bands, as illustrated by the sample spectrum (averaged over delays of 300 to 500 fs) shown as inset in Fig. 2B. Most prominently, one band is observed to shift to lower photon energies by 10 eV, terminating at 288 eV. Two further bands shift up and down by ~ 1 eV, respectively, and a fourth band appears as a shoulder of the absorption spectrum around 302 eV. A 50% fraction of the static CF_4 absorption spectrum has been subtracted from the whole data set (Fig. 2B) to account for partial ionization of the probed sample. This fraction has been obtained by comparing the absorption spectrum at long delays with calculated spectra of CF_3^+ . The delay in the appearance of the isolated absorption band of CF_3^+ has been determined by integrating the signal at each delay over a narrow energy range and fitting an error function to the time-dependent signal. This analysis reveals a time delay of (40 ± 2) fs in the appearance of the absorption band and provides a time resolution of (40 ± 5) fs (SOM, Section 2.2).

The observed changes in the absorption spectrum are the signature of symmetry lowering that occurs when the initially tetrahedral CF_4^+ molecule dissociates into the trigonal planar CF_3^+ molecule. Descent-in-symmetry arguments from group theory combined with dipole-selection rules show that a transition of the type $\text{C } 1s \rightarrow t_2$ in CF_4 must split into two transitions of the type $\text{C } 1s \rightarrow a_2''$ and $\text{C } 1s \rightarrow e'$ in CF_3^+ , as observed in Fig. 2B and illustrated in Fig. 2C.

Further insight is obtained by comparison with advanced quantum-chemical *ab-initio* calculations (stick spectrum in Fig. 2B and Fig. 3), which are further described in the supplementary online material (SOM, Section 3). The X-ray absorption spectrum of CF_4 is dominated by transitions to the $5t_2$ and $6t_2$ orbitals, which appear as two intense lines at the bottom of Fig. 3A. Along the reaction path, the transition to the $5t_2$ orbital first splits into transitions to three non-degenerate orbitals in CF_4^+ . This is the signature of the Jahn-Teller effect which causes the minimum-energy geometry to be of C_{2v} symmetry for short ($\leq 1.6 \text{ \AA}$) C-F bond lengths (27). With increasing bond length, the minimum-energy geometry changes to D_{3h} , which is accompanied by the merging of the second- and third-lowest transitions to a single line corresponding to a transition to the $5e'$ orbital, which confirms the symmetry arguments given in the preceding paragraph.

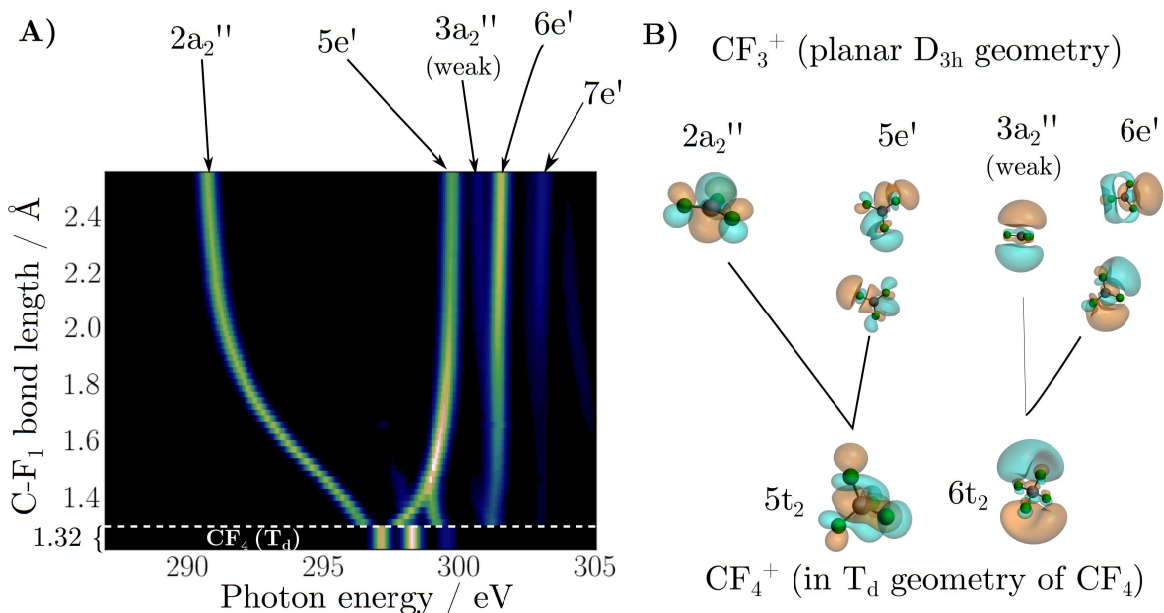


Figure 3: **Calculated X-ray absorption spectra of the reaction $\text{CF}_4^+ \rightarrow \text{CF}_3^+ + \text{F}$** A) X-ray absorption spectra, calculated with the TDDFT method using the LB94 functional and the QZ4P basis set, as a function of one C-F internuclear separation along the minimum-energy reaction path $\text{CF}_4^+ \rightarrow \text{CF}_3^+ + \text{F}$ calculated on the CCSD/6-31G* level of theory. The CF_4 X-ray absorption spectrum is shown below the dotted line. A linear intensity scale has been used. B) Unoccupied orbitals characteristic of the final state of the X-ray transition, corresponding to the dominant absorption bands of panel A. Only one of three equivalent orbitals is shown in the tetrahedral (T_d) geometry of CF_4^+ , whereas both, distinct orbitals of e' symmetry are shown for CF_3^+ .

Figure 3A also reveals a very large shift of the lowest-energy X-ray-absorption band occurring in the transition from CF_4^+ to CF_3^+ . The major part of this shift originates from the changing energy of the unoccupied $2a_2''$ orbital, caused by its evolution along the reaction path as shown in Fig. 3B. We next consider the complementarity of the intensity evolutions in the $5e'$ and $6e'$ transitions. In the tetrahedral geometry of CF_4 , the $5t_2$ orbital has dominant valence character, whereas the $6t_2$ orbital has dominant Rydberg character with most of its probability located outside the sphere defined by the fluorine atoms. This arises because the high electron density at the strongly electronegative fluorine atoms creates an effective potential barrier along the radial direction. This so-called "cage effect" has first been discussed in the context of XANES spectra of SF_6 to which we return below (28). As the CF_4^+ molecule dissociates, the fluorine cage opens up, going from a tetrahedral geometry to a planar one in CF_3^+ . This evolution causes

a mixing of Rydberg and valence character of the orbitals. Indeed, orbitals previously localized inside (valence) or outside (Rydberg) the cage display a mixed character after dissociation. This change causes a decrease of the overlap between the highly localized core orbital and the initially localized valence orbitals, translating into a decrease of their absorption as the cage opens. In contrast, Rydberg orbitals with initially small overlap with the core orbital exhibit an increase of their absorption as the cage opens up. Along the dissociation coordinate the 5e' orbital therefore develops partial Rydberg character, whereas the 6e' orbital acquires partial valence character (see Fig. 3B). This explains both the calculated and the observed intensity variations, i.e. a decreasing intensity for the transition leading to the 5e' orbital and an increase of the transition strength to the 6e' orbital. The appearance of the shoulder on the high-energy side of the absorption spectrum around 302 eV (Fig. 2B) is also reproduced by the calculations shown in Fig. 3A and is attributed to the 7t₂ orbital acquiring partial valence character as it evolves into the 7e' orbital of CF₃⁺.

The good agreement between experimental and theoretical results enabled us to reconstruct the average C-F internuclear separation as a function of time during the dissociation of CF₄⁺. These results are shown in Section 4.2 and Fig. S10 (SOM). Moreover, the analysis of time-dependent energy shifts of the 2a₂' absorption band provides evidence for the transient excitation of vibrational modes during the dissociation process (Section 4.3 and Fig. S11 in SOM).

We proceeded to demonstrate the generality of our technique by turning to the sulfur L-edges and studying the photodissociation SF₆⁺ → SF₅⁺ + F. The three lowest electronic states of SF₆⁺ of respective vertical ionization energies 15.7, 17.0 and 17.0 eV (measured as energy difference from the neutral ground state) (29), all dissociate to SF₅⁺ + F (26).

Figures 4B and 4C show the observed time-resolved XANES spectra following strong-field ionization of SF₆, observed at the L_{2,3}-edge and the L₁-edge of sulfur simultaneously. A 55% fraction of the static SF₆ absorption spectrum has been subtracted from the whole data sets (Figs. 4B and 4C) for clarity, for the same reason as in Fig. 2B. The L_{2,3}-XANES spectrum at negative delays is dominated by transitions from the sulfur 2p shell of SF₆ to the unoccupied orbital of a_{1g} symmetry, lying below the L_{2,3} edge, and to the shape resonances of t_{2g} and e_g symmetry lying above (see Fig. 4D). These shape resonances are confined by the effective potential barrier created by the presence of the surrounding electronegative fluorine atoms (28),

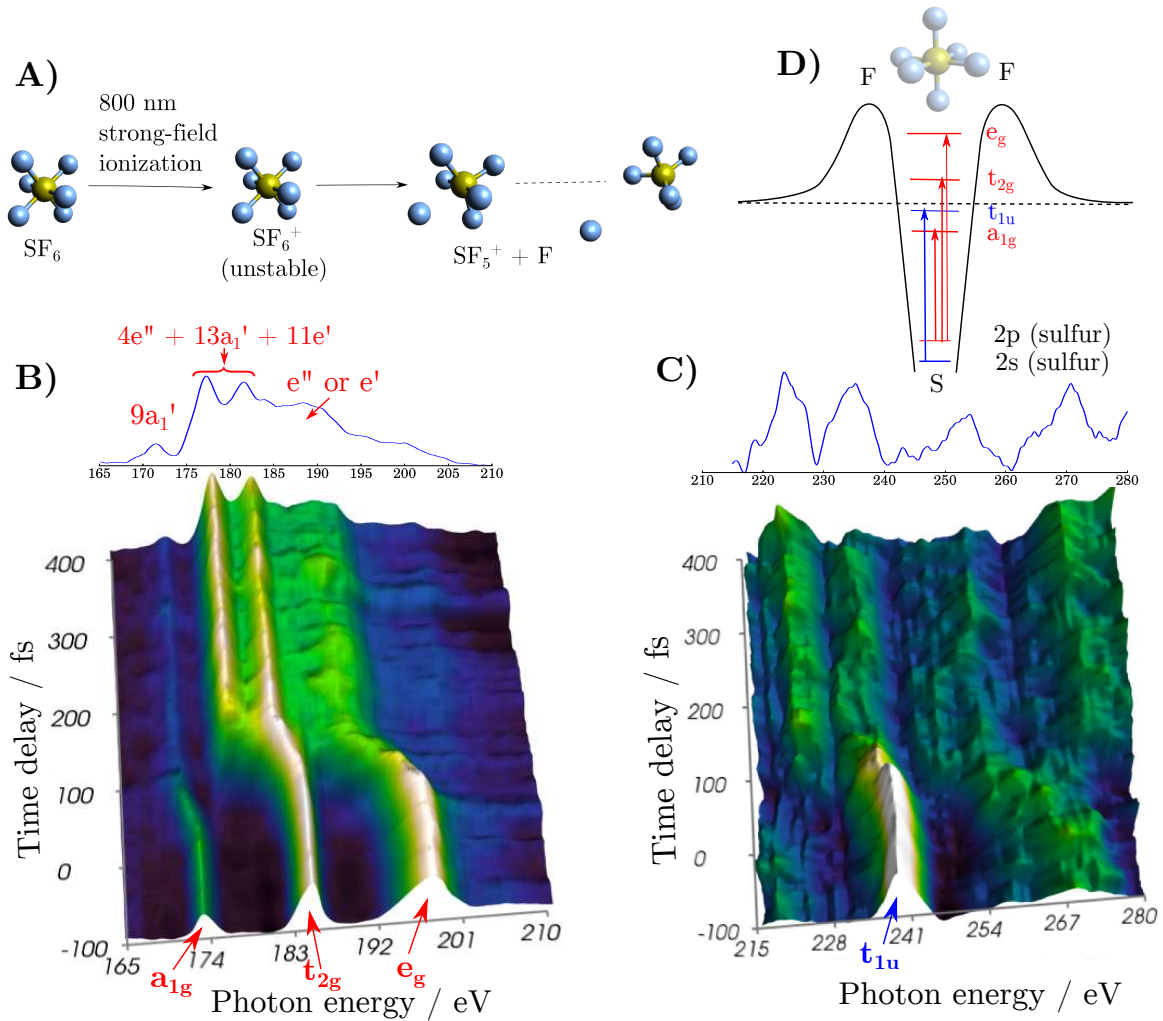


Figure 4: **Transient absorption spectroscopy at the sulfur L-edges** A) An intense infrared pulse induces single ionization of SF₆ to SF₆⁺ which is unstable in its electronic ground state and dissociates into SF₅⁺ + F. The sequence of geometries is taken from a calculated minimum-energy reaction path. B) Absorbance ($A(t) = \ln(I_0/I(t))$) at the L_{2,3}-edge as a function of the SXR-NIR time delay. Negative time delays correspond to the SXR pulse preceding the NIR pulse. The standard deviation of this data set amounts to 4.3%. C) Absorbance at the L₁-edge of SF₆. The insets show absorption spectra obtained by averaging over delays of 200-400 fs. All intensity axes shown in this figure, as well as all color scales, are linear. The standard deviation of this data set amounts to 6.3%. D) Orbital diagram illustrating the experimentally observed transitions.

as we have discussed in the case of CF₄. However, in SF₆, they are contained within the cage and therefore have considerable overlap with the central sulfur atom, which explains their strength in the experimental absorption spectra. The a_{1g} band shifts to lower energies by 2 eV, the t_{2g} band

splits into two main components that shift to lower energies by 2.5 and 6.5 eV, respectively, and the e_g band shifts to lower energies and broadens considerably. The red shift of all of these absorption bands is consistent with an increase of the local electron density on the sulfur atom, which is a consequence of the loss of an electron-withdrawing fluorine atom. The delay in the appearance of the absorption bands of SF_5^+ has been determined by integrating the signal at each delay over a narrow energy range and fitting an error function to the time-dependent signal. This analysis reveals time delays ranging from (34 ± 4) fs to (74 ± 10) fs in the appearance of the absorption bands and provides a time resolution of (45 ± 7) fs (SOM, Table S1 and Section 2.3). The absorption at the L_1 -edge (Fig. 4C) is dominated by the transition to a t_{1u} anti-bonding orbital, which is observable because of the *gerade* parity of the $2s$ initial orbital. This band splits into two main components that shift to lower energies by 6 and 15 eV, respectively.

The changes observed in the TR-XAS spectra of SF_6 can again be assigned by group theory. SF_6^+ in each of its lowest three electronic states can only dissociate into SF_5^+ in its electronic ground state, which has a trigonal bipyramidal geometry and belongs to the D_{3h} point group. By symmetry, the transition to the a_{1g} orbital of SF_6 should correlate with a transition leading to an a'_1 orbital in the D_{3h} point group of SF_5^+ . Similarly, the t_{2g} shape resonance of SF_6 will correlate with a'_1 and e' or e'' shape resonances in SF_5^+ . Finally, the e_g -symmetry shape resonance should correlate with an e' - or e'' -symmetric resonance in SF_5^+ . These symmetry correlations precisely describe the experimental observations. The absorption bands corresponding to the unoccupied a_{1g} orbital and the e_g shape resonance are both observed to shift to lower energies, without apparent sign of splitting. In contrast, the absorption band corresponding to the t_{2g} shape resonance is observed to split into two bands. Whereas the shift of all transitions happens almost simultaneously (SOM, Figs. S12 and S13), the splitting of the t_{2g} band is delayed by ~ 70 fs. Calculations (SOM, Section 5) suggest that this delayed splitting is caused by a higher sensitivity of the valence-type orbital characteristic of the t_{2g} shape resonance in SF_6 to bond angle changes, as compared to the a_{1g} and e_g orbitals (SOM, Fig. S16). The observed splitting of the absorption band would then be driven by rapid changes in bond angles of the SF_5^+ unit that occur around values of 2.5-3 Å for the SF_5^+ -F dissociation coordinate.

Qualitatively similar dynamics are observed at the L_1 edge. By symmetry, the dominant $2s \rightarrow t_{1u}$ transition can only split into two transitions leading to orbitals of e' or a''_2 symmetries,

which corresponds well to the experimental observation of a splitting into two bands. The broad absorption feature observed around 267 eV corresponds to several absorption bands, all located above the L_1 edge (244.17 eV). These bands correspond to shape resonances which have a very short lifetime and, therefore, a large natural linewidth leading to the observation of a single very broad absorption feature.

Our results demonstrate the feasibility of time-resolved XAS with table-top light sources and its potential in elucidating the dynamics of electrons and nuclei in chemical reactions. Specifically, this method nicely complements other key techniques in molecular reaction dynamics, such as time-resolved photoelectron spectroscopy (30) and time-resolved high-harmonic spectroscopy (31). We therefore anticipate TR-XAS to become a decisive technique for the investigation of non-adiabatic molecular dynamics, such as those occurring at conical intersections (32, 33). Owing to its sensitivity to elements, TR-XAS will enable time-resolved studies of electronic dynamics with atomic spatial sensitivity. Broadening the spectral coverage of our source only slightly would bring time-resolved extended X-ray absorption fine structure (TR-EXAFS) in combination with X-ray absorption near edge structure (XANES) experiments within reach, providing full structural and electronic information. A further improvement of the photon flux may bring non-linear X-ray spectroscopies within reach (34). Although demonstrated in the gas phase, our method is directly applicable to the solid state and is readily extendable to the liquid phase using flow cells (35) or flat microjets (36).

Acknowledgments

We thank Luigi Bonacina, Andres Laso, Andreas Schneider and Michel Moret for technical support, David Prendergast, Rock Bohinc and Jeroen van Bokhoven for helpful discussions on the calculation of soft-X-ray absorption spectra and Markus Reiher and Christopher Stein for performing supporting calculations. We gratefully acknowledge funding from the NCCR-MUST, a funding instrument of the Swiss National Science Foundation, an ERC Starting Grant (Project No. 307270-ATTOSCOPE) and an ERC Advanced Grant (Project No. 291201-FILATMO). Yoann Pertot thanks the ETH Zurich postdoctoral fellowship program for support.

Additional data supporting the conclusions are shown in the supplementary material.

References and Notes

1. M. H. F. Wilkins, A. R. Stokes, H. R. Wilson, *Nature* **171**, 738 (1953).
2. J. A. van Bokhoven, C. Lamberti, eds., *X-Ray Absorption and X-Ray Emission Spectroscopy: Theory and Applications* (John Wiley & Sons, 2016).
3. C. Bressler, *et al.*, *Science* **323**, 489 (2009).
4. W. Ackermann, *et al.*, *Nat Photon* **1**, 336 (2007).
5. P. Emma, *et al.*, *Nat Photon* **4**, 641 (2010).
6. T. Ishikawa, *et al.*, *Nat Photon* **6**, 540 (2012).
7. E. Allaria, *et al.*, *Nat Photon* **6**, 699 (2012).
8. F. Ráksi, *et al.*, *The Journal of Chemical Physics* **104**, 6066 (1996).
9. M. Bargheer, *et al.*, *Science* **306**, 1771 (2004).
10. C. Spielmann, *et al.*, *Science* **278**, 661 (1997).
11. E. Seres, J. Seres, F. Krausz, C. Spielmann, *Phys. Rev. Lett.* **92**, 163002 (2004).
12. E. Seres, C. Spielmann, *Applied Physics Letters* **91**, 121919 (2007).
13. E. J. Takahashi, T. Kanai, K. L. Ishikawa, Y. Nabekawa, K. Midorikawa, *Phys. Rev. Lett.* **101**, 253901 (2008).
14. M.-C. Chen, *et al.*, *Phys. Rev. Lett.* **105**, 173901 (2010).
15. T. Popmintchev, *et al.*, *Science* **336**, 1287 (2012).
16. N. Ishii, *et al.*, *Nat Commun* **5**, 3331 (2014).
17. S. L. Cousin, *et al.*, *Opt. Lett.* **39**, 5383 (2014).
18. F. Silva, S. M. Teichmann, S. L. Cousin, M. Hemmer, J. Biegert, *Nat Commun* **6**, 6611 (2015).

19. Z. H. Loh, *et al.*, *Phys. Rev. Lett.* **98**, 143601 (2007).
20. E. Goulielmakis, *et al.*, *Nature* **466**, 739 (2010).
21. M. Schultze, *et al.*, *Science* **346**, 1348 (2014).
22. A. R. Attar, A. Bhattacharjee, S. R. Leone, *The Journal of Physical Chemistry Letters* **6**, 5072 (2015).
23. K. Ueda, *et al.*, *Journal of Electron Spectroscopy and Related Phenomena* **79**, 441 (1996).
24. E. Hudson, *et al.*, *Phys. Rev. A* **47**, 361 (1993).
25. D. M. P. Holland, *et al.*, *Chemical Physics* **308**, 43 (2005).
26. J. Creasey, *et al.*, *Chemical Physics* **174**, 441 (1993).
27. J. M. García de la Vega, E. San Fabián, *Chemical Physics* **151**, 335 (1991).
28. J. L. Dehmer, D. Dill, S. Wallace, *Phys. Rev. Lett.* **43**, 1005 (1979).
29. D. M. P. Holland, *et al.*, *Chemical Physics* **192**, 333 (1995).
30. T. Suzuki, *Annu. Rev. Phys. Chem.* **57**, 555 (2006).
31. H. J. Wörner, J. B. Bertrand, D. V. Kartashov, P. B. Corkum, D. M. Villeneuve, *Nature* **466**, 604 (2010).
32. D. Polli, *et al.*, *Nature* **467**, 440 (2010).
33. H. J. Wörner, *et al.*, *Science* **334**, 208 (2011).
34. S. Mukamel, D. Healion, Y. Zhang, J. D. Biggs, *Annual Review of Physical Chemistry* **64**, 101 (2013). PMID: 23245522.
35. N. Huse, *et al.*, *Journal of the American Chemical Society* **132**, 6809 (2010).
36. M. Ekimova, W. Quevedo, M. Faubel, P. Wernet, E. T. J. Nibbering, *Structural Dynamics* **2**, 054301 (2015).